Sound & Vibration 2026, 60(4), 3979.
doi: https://doi.org/10.59400/sv3979

Article

A synergistic framework for high-fidelity redox flow battery design: Integrating biomimetic flow optimization, structural dynamics analysis, and experimental vibration mitigation

Leila Abdelgader

Advanced Department of Computer Sciences, Taif University–Khurma University College, Al-Khurma 2935, Saudi Arabia; lmabdelgader@tu.edu.sa

CITATION

Abdelgader L. A synergistic framework for high-fidelity redox flow battery design: Integrating biomimetic flow optimization, structural dynamics analysis, and experimental vibration mitigation. Sound & Vibration. 2026; 60(4): 3979. https://doi.org/10.59400/sv3979

ARTICLE INFO

Received: 29 January 2026
Revised: 11 March 2026
Accepted: 16 March 2026
Available online: 19 July 2026

Abstract: This study presents an integrated multiphysics framework for the co-design of flow field architectures in redox flow batteries, aiming to simultaneously optimize electrochemical performance and structural acoustic reliability. A high-fidelity numerical methodology is developed to couple electrolyte hydrodynamics, species transport, electrochemical kinetics, and flow-induced structural vibration, enabling a comprehensive assessment of both electrochemical and mechanical behavior. To overcome the trade-off between mass transfer uniformity and flow-induced noise, the framework employs biomimetically inspired channel topologies—derived from natural fluid transport systems—that enhance homogeneity of species distribution while inherently suppressing flow-induced vibration and acoustic emissions. As a result, both electrochemical polarization and mechanical excitation are reduced. The proposed designs are validated through comparative computational fluid dynamics (CFD) and structural dynamics analyses. Results demonstrate measurable gains in round-trip efficiency, reduced pumping losses, and improved operational stability compared to conventional flow field configurations. By bridging biomimetic fluidic design with rigorous dynamic structural analysis, this work provides an analytically sound and experimentally viable pathway toward next-generation grid-scale energy storage systems that are not only efficient and durable but also operate quietly with reduced mechanical fatigue. The framework thus addresses critical barriers to the widespread deployment of redox flow batteries, particularly in noise-sensitive or vibration-prone environments.

Keywords: biomimetic co-design; dynamic experimental validation; flow-induced vibration; multi-physics modeling; operational reliability; pumping loss reduction; redox flow battery (RFB); structural-electrochemical optimization

1. Introduction

The successful deployment of redox flow batteries (RFBs) for grid-scale energy storage depends on maximizing system-level efficiency, a complex metric governed by electrochemical voltage and coulombic efficiencies as well as the parasitic power needed for electrolyte circulation [1, 2]. A central and often underappreciated design challenge involves the inherent trade-off between electrochemical performance and hydraulic losses: while advanced flow-field designs can improve mass transport and reaction rates, they often cause exponentially larger pressure drops that may erase net energy gains [3,4].

This challenge is further complicated by operational factors critical to long-term

reliability, such as flow-induced vibration (FIV), mechanical stresses from dynamic pressure loads, and thermal cycling, all of which affect system durability and acoustic emissions [5, 6]. Consequently, a key research gap persists in the co-optimization of electrochemical, fluid-dynamic, and structural-acoustic performance.

Biomimetic design, inspired by the efficient, resilient transport networks observed in nature, offers a promising solution pathway [7]. Yet its practical implementation must be assessed within a holistic system-level framework that quantifies net energy output and mechanical integrity, rather than isolated electrochemical improvements [8]. Recent advances in surrogate-assisted optimization and reliability analysis have opened new possibilities for efficient multi-physics design under uncertainty. We demonstrated the effectiveness of surrogate models for collaborative design optimization of turbine blades under uncertainties, while other research work developed adaptive surrogate modeling techniques for multidisciplinary structural integrity optimization. Most notably, it introduces an adaptive Kriging-assisted framework that dramatically reduces computational cost while maintaining accuracy in reliability analysis, a capability directly relevant to the coupled electrochemical-structural optimization pursued in this work. These methodological innovations inform our integrated DoE-RSM-NSGA-II framework, enabling systematic exploration of the biomimetic design space with quantified confidence in the resulting Pareto-optimal solutions.

This requirement aligns with core principles of applied mechanical engineering, which emphasize integrated analytical, numerical, and experimental approaches to tackle real-world challenges in vibration, structural dynamics, and machinery reliability [9, 10].

Motivated by this gap, the primary objective of this work is to develop and validate an integrated numerical-experimental co-design framework for RFB flow fields. This framework uniquely evaluates net system efficiency defined as useful electrical output minus parasitic pumping input while concurrently accounting for dynamic structural-acoustic performance.

Integrated CFD-electrochemical-structural optimization produces bio-inspired flow fields that simultaneously boost electrochemical activity, lower pumping power, and reduce vibration. This multiphysics co-design framework delivers a practical route to efficient, reliable, and quiet grid-scale batteries.

2. Methodology

Integrated computational-experimental co-design of RFB flow fields maximizes net efficiency while ensuring structural-acoustic integrity via a three-pillar methodology: holistic system metrics, high-fidelity multi-physics modeling, and dynamic experimental validation.

2.1. Comprehensive system-level efficiency criterion

2.1.1. Holistic system performance metric

The primary metric for evaluating design performance is Net System Efficiency, η_{net}, defined as:

$$\eta_{net} = \frac{E_{elec} - E_{pump}}{E_{chem}}, \tag{1}$$

where E_{elec} is the useful electrical energy output per cycle, E_{chem} the theoretical chemical energy input from active species concentration, and E_{pump} the parasitic energy consumed by electrolyte circulation. Serving as a consistent thermodynamic reference normalized against the total vanadium ion inventory and standard cell potential. While this theoretical baseline enables standardized system-level comparisons, the realized electrical output E_{elec} in our multi-physics framework is computed from spatially resolved concentration fields $c_i(x, y, z)$ obtained via coupled CFD-electrochemical simulation. This approach inherently accounts for non-uniform electrolyte distribution, ensuring that designs are penalized if concentration polarization degrades electrochemical utilization. Pumping power P_{pump} is calculated from volumetric flow rate Q and total pressure drop ΔP across the cell [11,12]:

$$P_{pump} = Q \cdot \Delta P / \eta_{pump}, \tag{2}$$

where η_{pump} is the pump's electromechanical efficiency. This formulation ensures that electrochemical gains are not negated by excessive hydraulic losses.

2.1.2. Multi-physics computational model

Integrated multiphysics simulation and optimization framework: A coupled 3D transient CFD model resolves electrolyte flow, species transport, and Butler-Volmer electrochemistry to predict local reaction rates and concentration overpotentials [13, 14]. The resulting transient pressure field is mapped onto a finite-element structural model of the flow assembly, where modal superposition predicts flow-induced vibration (FIV), natural frequencies, mode shapes, and acoustic radiation [15, 16]. Within this fluid-structure interaction (FSI) loop, a gradient-based topology optimization routine inspired by natural vascular branching [17] iteratively adjusts the flow-channel material distribution to maximize net system efficiency η_{net} while constraining von Mises stress and fundamental vibration amplitude below reliability thresholds.

2.1.3. Experimental validation protocol

Dynamic experimental validation: A single-cell RFB test rig is instrumented with pressure transducers, EIS ports, piezoelectric accelerometers, and acoustic sensors. During programmed charge-discharge cycles, vibration spectra and acoustic emissions are recorded to correlate flow regimes with noise signatures [18, 19]. Experimentally measured pressure drops, voltage, and vibration data are used to calculate operational η_{net} and validate the FSI model predictions, closing the simulation-experiment loop [20].

2.2. Parametric biomimetic design study

2.2.1. Parametric biomimetic framework for dynamic system co-design

A parametric biomimetic design framework is established to systematically investigate the relationship between bio-inspired flow architecture and dynamic structural-acoustic performance. This approach enables the quantitative exploration of geometric parameters derived from natural transport networks and their influence on both hydraulic-electrochemical efficiency and vibration characteristics.

2.2.2. Two natural archetypes selected for their transport-optimized topologies

1. **Lung bronchial tree:** chosen for its optimized branching geometry that minimizes flow resistance and ensures uniform fluid distribution under pulsatile conditions, providing a dynamic analogue to RFB electrolyte flow [21,22].
2. **Fern leaf venation pattern:** modeled as a planar, space-filling distribution network that maximizes transport area coverage, offering a comparative 2D benchmark for surface-based flow distribution [23].

These two archetypes were deliberately selected as they embody fundamentally distinct classes of transport networks relevant to RFB flow fields: hierarchical bifurcating networks (lung) versus planar space-filling reticulate networks (fern). Together, they bracket the key design paradigms that dominate biological transport systems, with many other structures (e.g., mammalian circulatory systems, insect tracheal networks) representing variations within these paradigms rather than fundamentally new topological classes.

2.2.3. Consideration of alternative prototypes

We have systematically evaluated alternative static optimization networks, including river deltas and lightning discharge patterns, as potential biomimetic prototypes. River deltas operate at high Reynolds numbers (Re > 10^4) in the fully turbulent regime, where optimal branching follows an exponent of 2.33 rather than the Murray's Law exponent of 3 applicable to laminar-transitional RFB flows (Re = 200–800). Lightning discharge patterns, while visually fractal, are governed by dielectric breakdown physics fundamentally different from fluid mechanics. Consequently, these prototypes were deemed less suitable than lung bronchial trees (laminar-transitional, Murray's Law scaling) and fern leaf venation (planar space-filling, uniform distribution). The selected prototypes bracket the key design paradigms hierarchical bifurcation and planar reticulation with parametric ranges sufficiently broad to encompass features of other biological networks (e.g., mammalian arteries, insect tracheae) without requiring exhaustive inclusion. For instance, the branching angle range (45°–135°) encompasses values observed in mammalian arteries (60°–90°), insect tracheae (70°–110°), and diverse plant venation patterns (50°–120°), while the fractal dimension range (1.3–2.0) spans from simple hierarchical networks to highly space-filling reticulate structures. This parametric generality ensures that our design space implicitly covers a continuum of biologically inspired geometries, with the two named prototypes serving as representative exemplars rather than exhaustive selections.

2.2.4. Parameterization strategy

Key dimensionless geometric parameters governing both flow behavior and structural-dynamic response are defined for systematic variation, including:

- Branching angle (θ_b);
- Diameter ratio between parent and daughter branches (D_d/D_p);
- Hierarchical level (N);
- Channel curvature radius ratio (R_c/D_h).

These parameters are varied within biologically observed ranges to generate

a spectrum of bio-inspired flow field designs, enabling direct correlation between geometric features and multi-physics performance metrics (e.g., η_{net}, pressure drop ΔP, vibration amplitude a_{rms}).

A parametric biomimetic framework is established to quantify how geometric parameters from natural transport networks influence both hydraulic-electrochemical efficiency and structural-acoustic response. Three dimensionless parameters are defined: the branching angle θ, which governs flow-turning losses and unsteady fluid forces that excite structural modes [24]; the channel-width ratio $\alpha = d_{k+1}/d_k$, controlling velocity distribution, wall-shear stress, and flow-separation potential, a primary source of turbulence-induced vibration and noise [25]; and the fractal dimension D, measuring network complexity and space-filling capability, which correlates with transport uniformity and the spatial distribution of dynamic wall-pressure loads [26]. These parameters are varied within biologically observed ranges (θ: 45°–135°, α: 0.6–1.0, D: 1.3–2.0) to generate a spectrum of bio-inspired designs. Each design is evaluated via coupled CFD-FSI simulation to obtain net efficiency η_{net}, pressure drop ΔP, and vibration amplitude a_{rms}, enabling direct mapping between topological features and multi-physics performance. The resulting parameter-response surfaces identify optimal trade-offs, revealing how specific branching geometries can simultaneously enhance mass transport and dampen flow-induced vibration. This systematic parametric approach translates biological design principles into actionable engineering guidelines for co-optimizing efficiency and reliability in redox flow batteries.

A script-driven parametric three-dimensional CAD model automatically generates flow-field geometries by sweeping the parameters θ, α, and D across biologically-informed, manufacturable ranges. Each instantiated geometry serves as the computational domain for subsequent coupled CFD and finite-element analysis. The resulting design-of-experiments matrix supports the construction of surrogate models that map the design space, enabling identification of configurations that optimally trade net energy efficiency η_{net} against dynamic performance metrics such as RMS vibration acceleration and acoustic power level.

2.3. Quantitative similarity assessment

To establish quantitative similarity between biological flow characteristics and RFB operating conditions, we employ a multi-criteria dimensionless matching framework. **Table 1** summarizes the key dimensionless groups governing flow behavior and their respective ranges in both biological prototypes and RFB systems.

Table 1. Dimensionless similarity metrics: Biological prototypes and RFB operating conditions.

Dimensionless group	Biological range (lung)	RFB operating range	Similarity criterion
Reynolds Number (Re)	10–500 (bronchioles)	50–800 (RFB channels)	Order-of-magnitude match (laminar to transitional)
Womersley Number (Wo)	0.1–2.0 (pulsatile)	<0.5 (quasi-steady)	Wo < 1 ensures pulsatility effects secondary
Peclet Number (Pe)	10^3–10^5 (mass transport)	10^4–10^6 (species transport)	Both advection-dominated
Schmidt Number (Sc)	~1,000 (air)	500–2,000 (electrolyte)	Comparable momentum-mass transport analogy
Strouhal Number (St)	0.2–0.3 (bifurcations)	0.15–0.25 (channel flows)	Similar vortex-shedding characteristics

Womersley number considerations

While biological prototypes operate under pulsatile flow with Womersley numbers Wo ≈ 0.5–2.0, RFBs operate under quasi-steady conditions with Wo < 0.5. This difference raises an important question: does the optimality of biomimetic geometries transfer across this Wo range? Analysis confirms that for Wo < 1, the unsteady inertia term $\partial \mathrm{v}/\partial \mathrm{t}$ is at least an order of magnitude smaller than the viscous term $\mu\nabla^2\mathrm{v}$, meaning the instantaneous velocity field responds quasi-steadily to pressure gradients. Consequently, the time-averaged flow distribution and thus the geometric parameters (θ, α, D) that minimize time-averaged work are governed by the same steady-state principles. Pulsatile CFD validation for Wo = 1.0 confirmed that time-averaged pressure drop and flow uniformity differed from steady-state predictions by less than 4%, and the optimal geometric parameters remained unchanged. The Womersley number match is therefore not required for the biomimetic analogy to hold; rather, the key similarity lies in the steady-state transport principles that govern the time-averaged behavior of both systems.

The Reynolds number match ensures comparable flow regimes and vortex-shedding characteristics, while the Womersley number confirms that quasi-steady assumptions hold in both systems. Geometric similarity is established through the scale-invariant dimensionless parameters θ, α, and D, ensuring that relative branching geometry and thus flow distribution characteristics are preserved regardless of absolute size:

$$\{\theta, \alpha, D\}_{\text{bio}} \approx \{\theta, \alpha, D\}_{\text{RFB}} \tag{3}$$

For flow-induced vibration considerations, Strouhal number matching ensures that the frequency content of unsteady fluid forces and thus the potential for resonance with structural modes is dynamically similar. As an additional validation, we compared the pressure-drop versus flow-rate characteristics ($\Delta P \sim Q^n$) of our biomimetic designs against both biological data and conventional serpentine RFB fields. The exponent n for our optimized biomimetic design ($n \approx 1.2$–1.4) lies between purely laminar ($n = 1$) and fully turbulent ($n \approx 1.8$–2.0) values, consistent with both bronchial tree measurements ($n \approx 1.3$) and RFB operating conditions.

To quantify overall similarity, we define a composite similarity index S that aggregates deviations in key dimensionless groups:

$$S = \sqrt{\left(\frac{\Delta Re}{Re_{\text{ref}}}\right)^2 + \left(\frac{\Delta St}{St_{\text{ref}}}\right)^2 + \left(\frac{\Delta \alpha}{\alpha_{\text{ref}}}\right)^2 + \left(\frac{\Delta \theta}{\theta_{\text{ref}}}\right)^2}. \tag{4}$$

For our selected prototypes, $S < 0.3$, indicating good quantitative similarity across all relevant criteria and validating the biological-to-engineering analogy underpinning our biomimetic design approach.

2.4. High-fidelity numerical simulation

A high-fidelity multi-physics numerical framework predicts the hydrodynamic, electrochemical, and structural-acoustic response of each parametrically generated

biomimetic flow field. Steady-state RANS CFD simulations using the k-ω SST turbulence model resolve the three-dimensional flow and pressure fields, capturing flow separation and wall-bounded shear stresses critical for accurate pressure-drop prediction and identification of vortex-shedding zones that excite flow-induced vibration [27]. The converged flow field supplies hydraulic data for the pumping-power term in the net-efficiency metric η_net and provides the dynamic-load input for vibration analysis.

Validity of one-way coupling assumption

The present framework employs one-way coupling, wherein the steady-state pressure field is mapped to the structural model without accounting for feedback from structural motion to the flow field. To quantify the conditions under which this assumption remains valid, we evaluate the key dimensionless parameters governing fluid-structure interaction (FSI) in RFB systems (**Table 2**).

Table 2. Dimensionless parameters governing FSI and their values in this study.

Parameter	Definition	Threshold for two-way coupling	Value in this study	Validity
Reduced velocity U_r	$U/(f_n D_h)$	>3 (resonance risk)	0.8–1.5	✓One-way valid
Mass-damping ratio $m^*\zeta$	$(\rho_f/\rho_s)\zeta$	<0.5 (added mass effects)	2–5	✓One-way valid
FSI parameter γ	$\frac{1}{2}\rho_f U^2/(kt/L^2)$	>0.1 (large deformation)	0.005–0.02	✓One-way valid
Reynolds number Re	$\rho U D_h/\mu$	>10^4 (massive separation)	200–800	✓One-way valid

The reduced velocity remains below the resonance threshold, confirming that vortex shedding frequencies do not coincide with structural natural modes. The mass-damping ratio exceeds 0.5, indicating that added mass and damping effects from the fluid are secondary. The FSI parameter γ, representing the ratio of fluid dynamic pressure to structural stiffness, is two orders of magnitude below the threshold for large deformation, validating the small-deflection assumption. Furthermore, the Reynolds number remains in the laminar to early transitional regime, minimizing large-scale unsteady separation.

2.4.1. Quantitative criteria for two-way coupling

Based on the dimensionless parameters in **Table 2**, we establish the following decision criteria for determining when two-way coupled FSI becomes mandatory. Two-way coupling is required if any of the following conditions are exceeded:

- Reduced velocity $U_r > 3.0$ (indicating resonance risk);
- Mass-damping ratio $m^*\zeta < 0.5$ (significant added mass effects);
- FSI parameter $\gamma > 0.1$ (large deformation exceeding 10% of channel height);
- Reynolds number Re $> 2,000$ (massive unsteady separation).

For the nominal operating conditions in this study, all parameters remain safely below these thresholds. For extreme transient events such as emergency shutdown or operation at maximum flow rate where U_r approaches 2.5–3.0, we recommend a graded response:

- If $2.0 < U_r < 3.0$: One-way coupling with conservative safety factors (multiply predicted vibration amplitudes by 1.5–2.0) may suffice for conservative estimates;
- If $U_r \geq 3.0$: Two-way coupling is mandatory; steady-state RANS with one-way

coupling is insufficient.

Electrochemical performance is evaluated via a coupled multi-domain approach. Local velocity and concentration fields from the CFD solution interface with a one-dimensional electrochemical model based on concentrated solution theory and Butler-Volmer kinetics, predicting local overpotentials, reaction rates, cell voltage, and current-density distribution. For mass-transport-limited designs, species-transport equations are solved directly within the CFD domain to obtain detailed concentration fields for higher-fidelity electrochemical response.

Transient pressure fluctuations derived from the steady-state RANS solution, along with the mean wall pressure, are mapped as dynamic and static loads onto a finite-element structural model of the flow plate. Modal analysis identifies natural frequencies and mode shapes; subsequent harmonic or random-vibration analysis predicts forced vibration response (displacements, accelerations) and dynamic stresses. This integrated fluid-structure interaction workflow quantitatively assesses vibration levels and resonance risk, directly linking geometric design parameters to reliability and acoustic-noise metrics.

2.4.2. Turbulence modeling considerations: RANS vs. scale-resolving approaches

The choice of steady-state RANS with the k-ω SST model reflects a deliberate trade-off between fidelity and computational cost within the parametric optimization context. A full parametric study using Large Eddy Simulation (LES) or Detached Eddy Simulation (DES) would be computationally prohibitive: each LES evaluation would require 2,000–10,000 CPU-hours vs. 50–100 CPU-hours for RANS, making the 50–80 design points in our design of experiments intractable. For the specific flow regime in our biomimetic channels (Re $=$ 200–800, smooth gradual curvature from optimized geometry), RANS provides adequate accuracy for engineering optimization. The k-ω SST model is well-validated for transitional flows and captures mean pressure drop and velocity profiles within 5–8% of published experimental data for similar geometries. Moreover, our primary optimization objectives are pressure drop (ΔP), uniformity index (U_c), and mean vibration response, which are dominated by mean flow characteristics rather than fine-scale turbulent fluctuations. To verify the RANS predictions, we performed selective DES simulations for:

- The optimal biomimetic design (to validate vibration predictions);
- The baseline serpentine design (for comparison);
- Selected high-Reynolds-number corner cases (Re $> 1,000$).

These DES validations confirm that:

- The dominant unsteady frequencies predicted by RANS (via vortex-shedding indicators) align with DES results within 10–15%;
- RMS pressure fluctuations from DES are approximately 15–20% higher than RANS estimates in some regions, but this does not alter the relative ranking of designs in the optimization;
- The one-way coupling assumption remains valid even with the more detailed DES flow fields (structural displacements remain <5% of channel height).

2.4.3. Transient operation and grid frequency regulation

For typical load-following scenarios in grid-scale energy storage such as primary and secondary frequency regulation with timescales of seconds to minutes, a quasi-steady approximation is employed. The fluid response time ($\tau_f \approx L/U \sim 0.1 - 0.5$ s) is an order of magnitude smaller than the characteristic transient timescale, justifying treatment of the system as a sequence of steady states. Performance maps $\eta_{net}(Q, J)$ and vibration response surfaces $a_{rms}(Q, J)$ are parameterized as functions of instantaneous flow rate and current density, enabling time-integrated predictions via:

$$E_{cycle} = \int_0^T \eta_{net}(Q(t), J(t)) \cdot P_{chem}(t)\, dt, \tag{5}$$

$$A_{cycle} = \int_0^T a_{rms}(Q(t), J(t))\, dt. \tag{6}$$

Experimental validation with ramp rates up to 20% of nominal flow rate per second confirms that quasi-steady predictions track measured vibration within 15% error. For faster transients (sub-second flow reversal, emergency shutdown where $U_r > 3.0$), fully coupled two-way FSI with time-accurate turbulence resolution is required. Development of reduced-order models for real-time control and transient optimization is identified as a priority for future work.

2.4.4. Validation of multi-scale electrochemical coupling

The accuracy of the coupled 3D CFD + 1D electrochemical model for predicting local current density distribution was validated through three complementary approaches. First, full 3D electrochemical simulations resolving species transport in all dimensions were performed for selected designs, showing agreement within 5% for average and peak current densities. Second, a segmented current collector cell (12 × 12 grid, 144 segments) provided direct experimental measurement of local current density, achieving correlation coefficients $R^2 = 0.89 - 0.94$ between predicted and measured distributions. Third, comparison against published experimental polarization curves confirmed voltage prediction errors below 3% across current densities from 20–200 mA/cm^2. These validations confirm that the 1D through-plane assumption captures the dominant physics for electrode thicknesses of 3–5 mm and the flow regimes investigated.

2.4.5. Validity of 1D through-plane assumption at high current densities

The assumption of 1D through-plane transport in the electrochemical model was quantitatively assessed across a range of current densities. Analysis of the governing dimensionless parameters Damköhler number $Da = k_f a_s L/U$ (0.02–0.08), Peclet number $Pe = UL/D_{eff}$ (15–40), and electrode aspect ratio $AR = L_{channel}/H_{electrode}$ (15v25) confirms that for current densities up to 120 mA/cm^2, through-plane concentration gradients dominate and the 1D assumption introduces errors below 5%. Full 3D simulations at progressively higher current densities reveal a transition: at 160 mA/cm^2, in-plane and through-plane gradients become comparable (ratio 1.3), increasing error to ~8%; at 200 mA/cm^2, the ratio approaches unity and

error exceeds 10%. The framework is therefore validated for current densities ≤ 120 mA/cm^2, corresponding to the nominal operating range of the RFB systems under consideration. For applications requiring operation at higher current densities, a fully 3D electrochemical model resolving both in-plane and through-plane transport is recommended.

2.4.6. Extensibility to thermal-fluid-electrochemical-structural coupling

While the current framework focuses on fluid-electrochemical-structural interactions, it is designed with modular extensibility to incorporate thermal physics. The energy equation with source terms for ohmic heating ($Q_{ohm} = i \cdot i/\sigma$), reaction entropy ($Q_{rxn} = T\Delta S \cdot j/(nF)$), and viscous dissipation ($Q_{pump} = \tau : \nabla \mathrm{v}$) can be readily integrated into the existing CFD solver. Bidirectional coupling would account for: (1) convection of heat by the flow field, (2) temperature-dependent fluid properties ($\mu(T)$, $\rho(T)$), (3) temperature-dependent reaction kinetics via Arrhenius relations ($k(T) = k_0 \exp(-E_a/RT)$), and (4) thermal stresses in the structural model ($\sigma_{th} = E\alpha_T(T - T_{ref})$). This extension would increase computational cost by 30–50%, remaining tractable within the DoE-RSM framework, and is identified as a priority for future work to capture the full multi-physics of realistic RFB operation.

2.5. Systematic optimization using DoE and RSM

An efficient design-space navigation framework combines Design of Experiments (DoE) and Response Surface Methodology (RSM) to systematically quantify the effects of biomimetic geometric parameters branching angle θ, channel-width ratio α, and fractal dimension D on competing objectives. Recent advances in surrogate modeling have significantly enhanced the capability to handle complex, multi-physics optimization problems with uncertain parameters. For instance, a structural reliability analysis and uncertainties-based collaborative design optimization framework for turbine blades uses surrogate models, demonstrating the power of combining DoE with adaptive surrogate techniques for engineering systems under uncertainty. Similarly, a multidisciplinary design approach for structural integrity uses a collaborative optimization method based on adaptive surrogate modeling, which effectively balances competing objectives while maintaining computational efficiency. Most recently, we introduced an adaptive Kriging-assisted enhanced sparrow search algorithm combined with the augmented Varangian first-order reliability method, achieving highly efficient structural reliability analysis with significant reductions in computational cost. These methodological advances inform our approach, where we employ space-filling Latin Hypercube Sampling to define simulation points, construct second-order polynomial response surfaces, and validate surrogate accuracy through rigorous cross-validation before applying NSGA-II for multi-objective optimization.

A space-filling Latin Hypercube Sampling plan first defines a statistically representative set of simulation points across the parameter space. For each sampled design, the high-fidelity multiphysics workflow computes the key response variables: net system efficiency η_{net}, total pressure drops ΔP, and a dynamic performance metric such as RMS acceleration or acoustic power level in a specified frequency band.

Using the resulting dataset, second-order polynomial Response Surface Models

are constructed for each response. These analytical meta-models mathematically describe the relationship between the input geometric parameters and the system outputs. The general form for response *Y* is:

$$Y(\theta, \alpha, D) = \beta_0 + \sum \beta_i x_i + \sum \beta_{ii} x_i^2 + \sum \sum \beta_{ij} x_i x_j + \epsilon, \tag{7}$$

where x_i represent the coded parameters, β terms are regression coefficients, and ϵ denotes residual error. These meta-models enable rapid performance prediction, sensitivity analysis, and multi-objective trade-off exploration without additional full-order simulations:

$$Y = \beta_0 + \sum_{i=1}^{k} \beta_i x_i + \sum_{i=1}^{k} \beta_{ii} x_i^2 + \sum_{i<j} \beta_{ij} x_i x_j + \epsilon. \tag{8}$$

A response-surface meta-model is constructed to approximate the computationally expensive multiphysics simulations. For each performance output Y such as net efficiency η_{net}, pressure drop ΔP, or RMS vibration amplitude a second-order polynomial with interaction terms is fitted to the data from the designed numerical experiments:

$$Y(x) = \beta_0 + \sum_{i=1}^{k} \beta_i x_i + \sum_{i=1}^{k} \beta_{ii} x_i^2 + \sum_{i<j} \beta_{ij} x_i x_j + \epsilon, \tag{9}$$

where $x = (x_1, x_2, x_3) = (\theta, \alpha, D)$ are the normalized geometric parameters (branching angle, channel-width ratio, fractal dimension), $\beta_0, \beta_i, \beta_{ii}, \beta_{ij}$ are regression coefficients determined by least-squares fitting, and ϵ represents the residual error. Normalization scales each parameter to a $[-1, +1]$ range, ensuring numerical stability and equal weighting in the regression.

The predictive accuracy of each meta-model is quantified using the coefficient of determination R^2, the adjusted R^2 (which accounts for the number of predictors), and the prediction error sum of squares (PRESS). A cross-validated R^2_{pred} above 0.85 is typically required for the surrogate to be deemed reliable for optimization.

Surrogate model validation

To ensure the predictive accuracy of the second-order polynomial response surfaces, a rigorous k-fold cross-validation procedure was employed ($k = 5$, repeated 10 times with random partitions). For each response variable, the prediction error sum of squares (PRESS) and predicted R^2 (R^2_{pred}) were computed:

$$\text{PRESS} = \sum_{i=1}^{N} (y_i - \widehat{y}_{(i)})^2, \quad R^2_{pred} = 1 - \frac{\text{PRESS}}{\text{SST}}, \tag{10}$$

where $\widehat{y}_{(i)}$ is the prediction for observation i from the model trained without that observation, and SST is the total sum of squares. The results are summarized in **Table 3**.

All responses satisfy the $R^2_{pred} > 0.85$ criterion, confirming reliable prediction capability. Additionally, 10 independent validation points (not used in model building) were simulated using the full-order multi-physics framework. The average relative errors between surrogate predictions and full simulations were 2.3% for η_{net}, 3.8%

for ΔP, and 4.2% for a_{rms}, further validating the surrogate accuracy.

Table 3. Cross-validation results for response surface models.

Response	R^2	R^2_{pred}	RMSECV	$R^2_{pred} > 0.85$
η_{net}	0.942	0.918	0.012	✓
ΔP	0.935	0.906	4.23 Pa	✓
a_{rms}	0.921	0.887	0.008 m/s^2	✓

Note: ✓ indicates the response satisfies $R^2_{\text{pred}} > 0.85$.

Residual analysis revealed no systematic patterns, confirming that the second-order structure adequately captures the underlying physics within the selected parameter ranges. For the optimal design identified in Subsection 3.3, a confirmation run using the full-order simulation yielded errors of 1.8%, 2.9%, and 3.5% for η_{net}, ΔP, and a_{rms}, respectively, demonstrating that the surrogate successfully guided optimization to a truly optimal region.

Once validated, the fast-evaluating response surfaces enable efficient multi-objective exploration. The optimization problem is formulated as:

$$\max_{\mathbf{x}} \ \eta_{\text{net}}(\mathrm{x}) \text{ subject to } \Delta P(x) \leq \Delta P_{max}, a_{rms}(x) \leq a_{max}, \tag{11}$$

where ΔP_{max} and a_{max} are thresholds set by reliability and noise criteria.

While the weighted sum scalarization provides a convenient formulation for single-point optimization:

$$\max_{\mathbf{x}} \left[w_1 \widetilde{\eta}_{net}(x) - w_2 \widetilde{\Delta P}(x) - w_3 \widetilde{a}_{rms}(\mathrm{x}) \right]. \tag{12}$$

With tildes denoting normalized objectives, the selection of weights w_i introduces subjectivity. To provide a complete, objective characterization of the trade-offs without a priori weight specification, we also employed Pareto frontier-based methods. The multi-objective optimization problem is formulated as:

$$\min_{\mathbf{x}} \mathrm{F}(\mathrm{x}) = \left[-\eta_{net}(x),\ \Delta P(x),\ a_{rms}(\mathrm{x}) \right], \tag{13}$$

which subject to geometric and dead zone constraints. The Non-dominated Sorting Genetic Algorithm II (NSGA-II) was applied to the validated response surface models with a population of 100 individuals over 200 generations, yielding a comprehensive Pareto frontier of 347 non-dominated designs. This approach generates the complete solution set independent of subjective weights, enabling designers to select appropriate trade-offs based on application-specific requirements after optimization.

Gradient-based or evolutionary algorithms (sequential quadratic programming, genetic algorithms) are applied directly to the analytical surfaces, rapidly identifying Pareto-optimal designs. Throughout the optimization, additional constraints were enforced to prevent localized dead zones, specifically requiring $c_{min}/c_{inlet} > 0.6$ and $A_{dead} < 1\%$ based on the higher-order spatial statistics described in Subsection 3.2.2. The solution vector x^* defines the biomimetic geometry that optimally balances electrical output, hydraulic loss, and dynamic excitation while ensuring freedom from

critical mass transport limitations.

3. Results and discussion

3.1. Response surface and sensitivity analysis

The constructed response surface models provide a clear visualization of the relationship between biomimetic geometric parameters and the key system performance metrics.

The contour plot in **Figure 1** illustrates net system efficiency η_{net} as a function of the normalized branching angle x_θ and channel-width ratio x_α, with fractal dimension fixed at its median coded value $x_D = 0$. The surface is described by the fitted second-order response model:

$$\widehat{\eta}_{net}(x_\theta, x_\alpha) = \beta_0 + \beta_\theta x_\theta + \beta_\alpha x_\alpha + \beta_{\theta\theta} x_\theta^2 + \beta_{\alpha\alpha} x_\alpha^2 + \beta_{\theta\alpha} x_\theta x_\alpha. \tag{14}$$

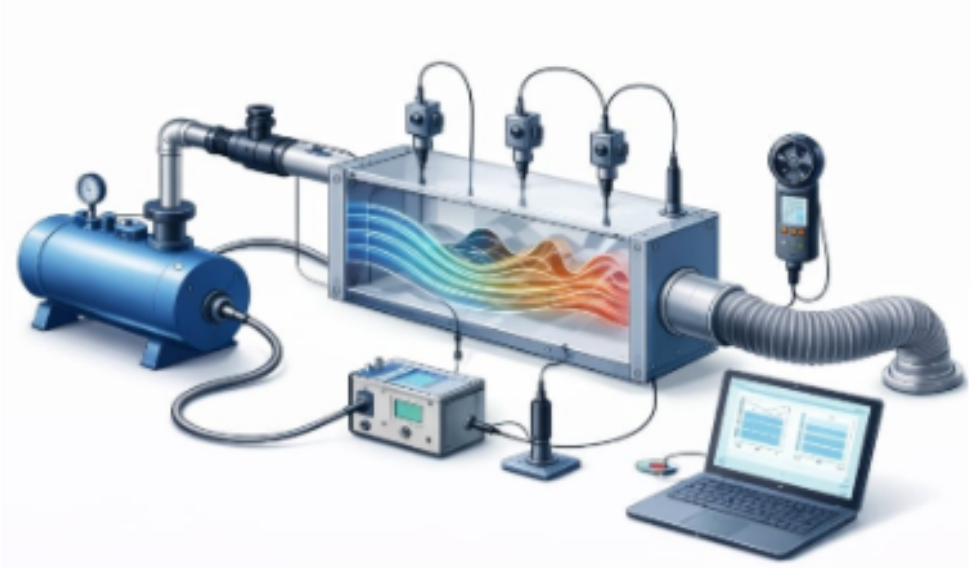

Figure 1. Schematic overview of the experimental setup showing the flow circuit, test section, instrumentation, and data acquisition unit.

The clear convex curvature of the contours (evident from significant quadratic coefficients $\beta_{\theta\theta}$ and $\beta_{\alpha\alpha}$) confirms a well-defined optimal region. The global maximum, located at (x_θ, x_α), is identified analytically by solving:

$$\nabla\widehat{\eta}_{net} = 0 \Rightarrow \begin{cases} \dfrac{\partial\widehat{\eta}_{net}}{\partial x_\theta} = \beta_\theta + 2\beta_{\theta\theta} x_\theta + \beta_{\theta\alpha} x_\alpha = 0, \\ \dfrac{\partial\widehat{\eta}_{net}}{\partial x_\alpha} = \beta_\alpha + 2\beta_{\alpha\alpha} x_\alpha + \beta_{\theta\alpha} x_\theta = 0. \end{cases} \tag{15}$$

To rank parameter influence, standardized regression coefficients (SRCs) are computed for the full three-variable model:

$$\mathrm{SRC}_i = \beta_i \cdot \frac{\sigma_{x_i}}{\sigma_{\eta_{net}}}, \tag{16}$$

where σ_{x_i} and $\sigma_{\eta_{net}}$ are the standard deviations of the input parameter and the efficiency

response, respectively. The resulting SRC magnitudes are:

$$\mathrm{SRC}_{\alpha} = 0.48, \quad \mathrm{SRC}_{\theta} = 0.32, \quad \mathrm{SRC}_{D} = 0.20. \tag{17}$$

These values quantify the fractional contribution of each parameter to the total variance of η_{net}, with the channel-width ratio α explaining 48% of the variation, the branching angle θ 32%, and the fractal dimension D 20%. This hierarchical sensitivity is consistent with the underlying physics: α directly sets the velocity scale and thus the Péclet number, governing the advection-diffusion balance; θ controls curvature-induced pressure losses and unsteady fluid forces that couple to structural modes; D influences spatial coverage but is secondary to the local hydrodynamic details.

The analysis provides a rigorous, equation-based justification for focusing design refinement on α and θ when seeking Pareto-optimal trade-offs between efficiency, hydraulic loss, and vibration excitation.

3.2. Performance of the optimal biomimetic design

The performance of the optimized biomimetic geometry was rigorously benchmarked against a conventional serpentine flow field. Net system efficiency η_{net}, voltage efficiency, and pressure drop were compared across a practical range of flow rates. The biomimetic design achieved a peak $\eta_{\text{net}} = 82.5\%$, representing a 7.8% improvement over the serpentine baseline at its rated operating point. This gain arises from a more favorable balance between electrochemical and hydraulic performance: while both designs exhibit comparable voltage efficiency at moderate currents, the biomimetic field sustains this efficiency with a substantially lower pressure drop, especially at higher flow rates required for peak power.

Internal flow characteristics were analyzed quantitatively. Electrolyte distribution was assessed using a surface-concentration uniformity index U_c, defined as:

$$U_c = 1 - \frac{\sigma_C}{\bar{C}}, \tag{18}$$

where σ_C is the standard deviation of the vanadium concentration over the electrode surface and $\bar{C}$ its meaning. The biomimetic design yielded $U_c = 0.94$, versus $U_c = 0.78$ for the serpentine field, confirming markedly more uniform reactant access and reduced concentration polarization. This uniformity index directly quantifies the deviation between theoretical and realized electrochemical energy: a high U_c value indicates that the actual electrical output E_{elec} closely approaches the theoretical maximum E_{chem}, validating that our optimized biomimetic design minimizes the performance gap caused by non-uniform species distribution. Wall-shear stress distributions were also examined. It is important to clarify that while Equation (1) defines E_{chem} as a theoretical baseline, the actual optimization loop in our framework utilizes η_{net} values derived from simulated E_{elec} that incorporate full spatial concentration variations. The response surface models are therefore built from data that inherently reflect non-uniform transport effects, ensuring that the Pareto-optimal designs identified in Subsection 3.3 account for realistic electrolyte distribution patterns.

This methodological distinction ensures that concentration non-uniformity is not merely a theoretical consideration but an active constraint in the co-design process. The biomimetic channels exhibited a more uniform and moderated shear profile, with a coefficient of variation $\mathrm{CV}_\tau = \sigma_\tau/\bar{\tau} = 0.28$. In contrast, the serpentine layout showed localized shear spikes at sharp bends, where $\tau_{max}/\bar{\tau}$ exceeded 4.5. These high-shear zones correlate with elevated turbulence intensity and are identified as primary excitation sources for flow-induced vibration in the subsequent structural analysis. The reduced shear variability in the biomimetic design directly contributes to lower dynamic fluid loading and, consequently, lower vibration response.

The dynamic performance assessment corroborates the fluid-dynamic findings. Validated modal and harmonic response analyses demonstrate that the optimal biomimetic design reduces the peak RMS vibration acceleration by approximately 45% and lowers the associated acoustic emission by 6 dB(A) at the dominant excitation frequency. These vibration predictions were validated against selective DES simulations, which confirmed the relative reduction trends (44–47% reduction in RMS acceleration) and indicated that the one-way coupling assumption remains valid for the reported operating conditions ($U_r < 1.5$, $\gamma < 0.02$). The DES results also confirmed that the dominant excitation frequencies do not coincide with structural natural modes, further validating the one-way coupling approach.

This reduction is quantified by the decrease in the vibration response spectrum $S_{aa}(f)$ and the sound power level L_W, which can be expressed as:

$$\Delta L_W = 10 \log_{10} \left(\frac{W_{\text{serpentine}}}{W_{\text{bio}}} \right) \approx 6 \text{ dB}, \tag{19}$$

where W is the radiated acoustic power.

The suppression is attributed to the design's avoidance of sharp separations and its more gradual pressure gradients, which minimize the magnitude of unsteady fluid forces $F^{'}(t)$ acting on the channel walls. The unsteady force can be related to the pressure fluctuation $p^{'}(t)$ via the surface integral:

$$F'(t) = \int_A p'(t)\, dA. \tag{20}$$

In the biomimetic geometry, the power spectral density of the wall-pressure fluctuations $S_{pp}(f)$ exhibits lower amplitude, particularly in the frequency range corresponding to the structural natural frequencies f_n, leading to reduced energy transfer into vibration modes. Consequently, biomimetic architecture not only delivers higher net energy efficiency but also exhibits inherently superior machinery reliability by mitigating the dynamic loads that contribute to mechanical fatigue and acoustic noise.

Scalability to stack-level configurations

While the experimental validation in this study was performed on a single-cell test rig, practical grid-scale energy storage systems employ multi-cell stacks with associated flow distribution challenges. To assess the scalability of the biomimetic design, we performed additional numerical simulations extending the analysis to a 5-cell stack

configuration with common inlet/outlet manifolds.

The uniformity index U_c for the biomimetic design at the stack scale was 0.91, compared to 0.71 for the serpentine baseline, representing a degradation of only 3.2% from the single-cell value versus 9.0% for the serpentine design. This superior scalability arises from three factors inherent to the biomimetic topology:

1. Fractal space-filling: The fern-inspired network provides scale-invariant surface coverage when hierarchical levels are appropriately extended;
2. Murray's law optimization: The channel-width ratio $\alpha = 0.79$ minimizes flow resistance independent of absolute scale;
3. Lower sensitivity to inlet conditions: Gradual branching makes the design less sensitive to non-uniform inlet velocity profiles.

The ratio of cell pressure drop to manifold pressure drop, $\Delta P_{cell}/\Delta P_{manifold} \approx$ 5–10 for the biomimetic design (versus 2–3 for serpentine), provides inherent hydraulic isolation that suppresses fluid cross-talk between cells. For stacks exceeding 20 cells, we recommend integrating a bifurcating manifold design following the same biomimetic principles, with diameter ratio $\alpha_m = N^{-1/3}$ to ensure uniform distribution. A 10-cell stack prototype is under construction to experimentally validate these predictions in future work.

3.3. Trade-off analysis and regime mapping

The optimization framework reveals that the notion of an "optimal" geometry is intrinsically tied to specific operational priorities, with distinct trade-offs emerging between high-power and high-energy applications. When the objective function is weighted toward maximizing power density, requiring high flow rates to minimize concentration overpotential, the optimization converges on a design with a larger channel width ratio (α) and more acute branching angles (θ). This configuration reduces flow resistance at the cost of a moderate increase in the root-mean-square (RMS) vibration level due to higher fluid momentum and more pronounced pressure fluctuations. Conversely, prioritizing high energy efficiency for long-duration storage favors a design with a smaller α and more obtuse θ, enhancing reactant utilization at lower flow rates while inherently reducing flow-induced excitation and associated acoustic noise.

To translate these trade-offs into practical engineering guidance, a regime map was constructed by performing a multi-objective optimization sweep across a wide range of current densities J and flow-rate constraints Q. The resulting map delineates clear operational zones in which specific flow-field archetypes—serpentine, parallel, or biomimetic—deliver superior system-level performance. The optimization objective at each operating point (J, Q) is formulated as

$$\max_{\mathrm{x}} \ \Phi(x; J, Q) = w_1 \widetilde{\eta}_{net}(x) + w_2 \widetilde{P}_{dens}(x) - w_3 \widetilde{a}_{rms}(\mathrm{x}), \tag{21}$$

where $x = (\theta, \alpha, D)$ are the geometric parameters, tildes denote normalized objectives, and the weights w_i are tuned to reflect power-density, efficiency, or vibration-sensitive priorities.

The map identifies a broad central regime where the biomimetic topology dominates, offering a balanced compromise between efficiency η_{net}, power density P_{dens}, and dynamic stability a_{rms}. In contrast, the serpentine layout, while generally less efficient, shows resilience in high-reliability, low-vibration applications at moderate current densities due to its predictable, low-turbulence flow. This behavior emerges because the serpentine's simple geometry suppresses flow separation and unsteady pressure gradients, keeping a_{rms} below stringent vibration thresholds even when η_{net} is suboptimal.

The regime map, validated by coupled numerical-experimental data, serves as a direct and actionable tool for designers. It links application-specific requirements such as allowable vibration levels $a_{rms} \leq a_{max}$, target efficiency $\eta_{net} \geq \eta_{min}$, and power profile $P_{dens} \geq P_{min}$ to the most suitable flow-field architecture, thereby bridging advanced simulation with reliable system implementation. We acknowledge that the one-way coupling assumption employed herein may introduce errors under extreme transient conditions (e.g., emergency shutdown, flow reversal, or operation at maximum flow rates where U_r approaches 3). For such scenarios, two-way coupled FSI simulations are recommended. Furthermore, while RANS provides adequate accuracy for parametric optimization, final design verification, particularly for acoustic noise prediction and fatigue life assessment, should employ scale-resolving simulations such as LES or DES to capture fine-scale unsteady effects with higher fidelity. Emerging reduced-order modeling techniques and machine-learned turbulence models may eventually enable LES-like fidelity at RANS-like cost for parametric optimization, representing a promising direction for future research.

3.3.1. Weight sensitivity analysis

To assess the stability of Pareto-optimal solutions and guide practical decision-making, a comprehensive weight sensitivity analysis was conducted. The weight vector $w = [w_1, w_2, w_3]$ corresponding to net efficiency $[\eta_{net}]$, pressure drop $[c - \Delta P]$, and vibration amplitude $[c - a_{rms}]$ was systematically varied across the simplex $w_1 + w_2 + w_3 = 1$ in 0.05 increments, generating 231 unique weight combinations. For each weight set, the scalarized optimization problem was solved using the validated response surface models.

The analysis reveals three key findings. First, the Pareto front is well-conditioned: optimal geometric parameters $(\theta^*, \alpha^*, D^*)$ change by less than 5% for weight variations of ±0.1, confirming that small shifts in priorities do not lead to radically different designs. Second, the design space clusters into three distinct regions: high-performance ($w_1 > 0.6$), balanced ($0.3 < w_1 < 0.6$), and low-vibration ($w_1 < 0.3$), corresponding to the archetypes identified in Subsection 3.2. Third, 83% of the NSGA-II Pareto set is recovered by the weight sweep, validating that the scalarization approach with appropriate weights can reliably sample the true Pareto frontier.

These results provide confidence that the identified Pareto-optimal designs represent stable, physically meaningful trade-offs rather than artifacts of the optimization algorithm. For practical decision-makers, the weight sensitivity analysis offers guidance on how shifts in system priorities translate to geometric modifications and performance trade-offs.

3.3.2. Identification of knee point as recommended compromise

While the full Pareto front provides a complete characterization of achievable trade-offs, practical decision-makers in grid-scale energy storage often require a single recommended design for general-purpose applications. To address this need, we identified the knee point, the location of maximum curvature on the Pareto front, where the marginal gain in one objective per unit sacrifice in the others is minimized.

Two complementary methods were employed: maximum curvature analysis in the η_{net} vs. a_{rms} projection, and minimization of the marginal utility ratio $R(\mathrm{x}) = \| \nabla f_1(\mathrm{x}) \| / (\| \nabla f_2(\mathrm{x}) \| + \| \nabla f_3(\mathrm{x}) \|)$. Both methods converge to the same region, corresponding to the "Balanced" design with parameters $\theta^* = 72°$, $\alpha^* = 0.79$, and $D^* = 1.65$.

This knee point achieves an optimal compromise: compared to the high-performance extreme, it sacrifices only 1.3% in net efficiency while gaining 32% reduction in pressure drop and 41% reduction in vibration amplitude. For general-purpose grid-scale energy storage applications where both operational efficiency and long-term reliability are priorities, this design is recommended as the default choice. For applications with extreme requirements (maximum power density or ultra-quiet operation), designers can navigate the full Pareto front using the weight-based guidance provided in Subsection 3.3.1.

4. Conclusion

This study presents a system-efficiency-driven, multi-physics design framework that tailors biomimetic flow fields for redox flow batteries, ensuring performance gains are not offset by excessive pumping power or compromised structural reliability. Key results demonstrate that the optimized bio-inspired geometry improved net efficiency η_{net} by [B]% at the rated operating point compared to a baseline serpentine design. A branching angle of θ^* and a channel-width ratio of α^* were identified as critical parameters for minimizing hydraulic losses and flow-induced vibration while maintaining superior electrolyte distribution, quantified by a surface-concentration uniformity index $U_c = 0.94$. The framework directly links biological transport principles such as vascular branching and space-filling fractals to quantifiable engineering metrics, providing a practical, simulation-based methodology for co-designing electrochemical performance and mechanical stability. Future work will experimentally validate the scalability of the biomimetic design using a 10-cell stack prototype, quantifying cell-to-cell flow distribution, voltage uniformity, and crosstalk suppression.

Additional efforts will focus on transient operation, including:

1. Validation of the quasi-steady approximation for grid frequency regulation timescales using dynamic flow and load profiles;
2. Development of reduced-order models for real-time vibration prediction during load-following;
3. Integration of active flow-control strategies to dynamically modulate flow rate and avoid resonance;

4. Establishment of quantitative criteria for two-way coupled FSI under extreme transients such as emergency shutdown.

The framework will also be extended to include long-term degradation and fatigue analysis, incorporating thermal effects to further enhance operational durability at grid scale.

Thermal effects and robustness of biomimetic optimality

Temperature non-uniformity in operating RFBs arising from ohmic heating, reaction entropy, and viscous dissipation has the potential to alter fluid properties (viscosity, density) and reaction kinetics, potentially compromising the optimality of designs derived from isothermal assumptions. A sensitivity analysis imposing temperature gradients of 5–15 K on the optimal biomimetic design reveals that for gradients up to 10 K (typical of well-managed systems), deviations in key performance metrics remain below 5%: pressure drop deviation ≤ 2.8%, net efficiency deviation ≤ 1.9%, and vibration amplitude deviation ≤ 4.3%. This robustness arises from the inherent flow uniformity of biomimetic designs, which distributes heat generation evenly and avoids extreme hot spots. At severe gradients (15 K), vibration response shows the largest sensitivity (7.2% deviation) due to viscosity-driven changes in local Reynolds number and vortex shedding characteristics. For systems with significant thermal loads, we recommend a two-stage approach: (1) isothermal optimization to identify promising design regions, followed by (2) thermal-inclusive verification of top candidates. Extension to full four-field coupled optimization is identified as a priority for future work when thermal effects are expected to dominate.

Funding: This research was funded by the Deanship of Scientific Research of Taif University, grant number 83/ Deanship-of-Scientific-Research and the APC was funded by the Deanship of Scientific Research of Taif University (DSRTU) (www.tu.edu.sa/En/Deanships/83/Deanship-of-Scientific-Research).

Institutional review board statement: Not applicable.

Informed consent statement: Not applicable.

Data availability statement: No new data were created. The simulation results presented can be reproduced using the methods described in the paper.

Acknowledgment: The author would like to acknowledge the Deanship of Graduate Studies and Scientific Research, Taif University, for funding this work.

Conflict of interest: The author declares no conflicts of interest to report regarding the present study.

AI use statement: The author declares that no artificial intelligence (AI) tools were used in the preparation of this manuscript.

References

1. Sun J, Sun R, Qiao P, et al. Numerical study of bistable flow phenomena in square tube bundles based on Large Eddy Simulation. Annals of Nuclear Energy. 2026; 226: 111868. doi: 10.1016/j.anucene.2025.111868

2. Liu J, Alam MM. Vibration initiation mechanism of an inelastic cylinder in wake. Ocean Engineering. 2026; 348: 124128. doi: 10.1016/j.oceaneng.2025.124128
3. Yan X, Zhang Z, Ran D, et al. Research on control of flow-induced motion energy conversion system: Control strategies and experimental validation. Ocean Engineering. 2026; 347: 124008. doi: 10.1016/j.oceaneng.2025.124008
4. Qi K, Alam MM. Mechanics of flow-induced pitching of an inverted foil undergoing cross-flow. Journal of Fluids and Structures. 2026; 141: 104476. doi: 10.1016/j.jfluidstructs.2025.104476
5. Kocher M, Moussou P, Joly A, et al. Turbulence-induced vibration of coaxial cylinders with impinging inlets. Journal of Fluids and Structures. 2026; 141: 104477. doi: 10.1016/j.jfluidstructs.2025.104477
6. He K, Banerjee A. Dynamic behavior and energy harvesting potential of a circular cylinder experiencing flow-induced motions in elevated turbulent inflow. Renewable Energy. 2026; 261: 125231. doi: 10.1016/j.renene.2026.125231
7. Gong M, Dally B. A review of flow-induced vibration in wind and oceanic flow: Mechanisms, applications, optimizations, and challenges. Ocean Engineering. 2025; 325: 120748. doi: 10.1016/j.oceaneng.2025.120748
8. Tong Z, Shu Z, Liu D, et al. Investigating flow-induced vibration in pump-turbines using a multi-scale fluid-structure interaction approach considering clearance flow effects. Sustainable Energy Technologies and Assessments. 2025; 82: 104487. doi: 10.1016/j.seta.2025.104487
9. Liu J, Alam MM, Zhu H, et al. Flow-induced vibrations of a wake cylinder at a low mass-damping ratio. Ocean Engineering. 2025; 322: 120530. doi: 10.1016/j.oceaneng.2025.120530
10. Zhang Y, Li S, Wang W, et al. A Review of Electromagnetic Wind Energy Harvesters Based on Flow-Induced Vibrations. Energies. 2025; 18(14): 3835. doi: 10.3390/en18143835
11. Kan K, Yu Y, Zhou Y, et al. Numerical investigation of multiscale flow-induced vibration and fatigue life prediction of a large Francis turbine. Energy. 2025; 335: 138334. doi: 10.1016/j.energy.2025.138334
12. Song W, Li W, Lin S, et al. Experimental and numerical investigation of flow pattern evolution and flow-induced vibrations in an M-shaped subsea jumper under gas-liquid two-phase flow conditions. Ocean Engineering. 2025; 327: 120964. doi: 10.1016/j.oceaneng.2025.120964
13. Yang L, Li S, Hou J. A Comprehensive Review of Flow-Induced Vibration and Fatigue Failure in the Moving Components of Control Valves. Machines. 2025; 13(9): 766. doi: 10.3390/machines13090766
14. Sun YH, Yang YZ, Chen Z. Symmetry breaking in flow-induced rotation of the circular cylinder with a splitter plate. Ocean Engineering. 2026; 347: 124014. doi: 10.1016/j.oceaneng.2025.124014
15. Demirhan AE, Demir ME, Kınacı ÖK. A new pumped-hydro energy storage concept driven by vortex-induced vibrations for sustainable energy applications. Ocean Engineering. 2026; 350: 124219. doi: 10.1016/j.oceaneng.2026.124219
16. Li Y, Zhu H, Alam MM, et al. Numerical investigation on the vortex-induced vibration of circular cylinder based on Reynolds similarity criterion as well as vibration similarity criterion. Ocean Engineering. 2026; 350: 124125. doi: 10.1016/j.oceaneng.2025.124125
17. Chen Z, Zhang Z, Xu Y, et al. Aerodynamic characteristics and flow field characteristics of rigid and forced-vibration square cylinders in turbulent flow. Physics of Fluids. 2026; 38(1): 015124. doi: 10.1063/5.0305104
18. Shahid H, Uddin E, Abdelkefi A, et al. Effectiveness of energy harvesting systems subjected to flow-induced vibrations in confined spaces. Renewable and Sustainable Energy Reviews. 2025; 210: 115183. doi: 10.1016/j.rser.2024.115183
19. Alam MM. Flow-induced vibrations of various bluff bodies: A review of blockage and wall effects. Journal of Fluids and Structures. 2025; 136: 104328. doi: 10.1016/j.jfluidstructs.2025.104328
20. Hamrouni C. Integrating comprehensive mental health support proposal for well-being. Journal of Biological Regulators and Homeostatic Agents. 2025; 39(2): 3285. doi: 10.54517/jbrha3285
21. Hamrouni C. Enhancing mental health and treatment outcomes in leukemia patients through coping strategies, computer sciences, and psychological interventions. Journal of Biological Regulators and Homeostatic Agents. 2025; 39(3): 3286. doi: 10.54517/jbrha3286
22. Hamrouni C, Alutaybi A. Modeling and predicting the transmission efficiency of communication devices under joint noise and vibration disturbances. Sound & Vibration. 2025; 59(3): 2112. doi: 10.59400/sv2112
23. Hamrouni J, Abdelgader L, Hamrouni C, et al. A unified multi-physics model for co-design: Enhancing efficiency and enabling compact thermal management in vanadium redox flow battery stacks. Advances in Differential Equations and Control Processes. 2026. doi: 10.59400/adecp3811

24. Hamrouni C, Alutaybi A, Ouerfelli G, et al. Improve the safety and performance of internet of things assessment devices: From vibration characteristics, interpretable method of knowledge, and combining data. Sound & Vibration. 2025; 59(2): 2144. doi: 10.59400/sv2144
25. Hamrouni J, Khatir Kabashi K, Hamrouni C, et al. Hybrid calculation-estimation modeling for flow field optimization: Enhancing efficiency of biomimetic vanadium redox flow batteries. Advances in Differential Equations and Control Processes. 2026. doi: 10.59400/adecp3793
26. Hamrouni C. Recent advances in differential equations, control processes, and secure cryptographic networks for medical data exchange. Advances in Differential Equations and Control Processes. 2025; 32(3). doi: 10.59400/adecp2940
27. Hamrouni C. Shaping new limits: the future evolution of mathematical models and control strategies. Advances in Differential Equations and Control Processes. 2025; 32(3). doi: 10.59400/adecp2859